

Minimally Deformed Regular Bardeen Black Hole Solutions in Rastall Theory

M. Sharif¹ * and Malick Sallah^{1,2} †

¹ Department of Mathematics and Statistics, The University of Lahore
1-KM Defence Road Lahore-54000, Pakistan.

² Department of Mathematics, The University of The Gambia,
Serrekunda, P.O. Box 3530, The Gambia.

Abstract

In this study, we utilize the minimal geometric deformation technique of gravitational decoupling to extend the regular Bardeen black hole, leading to the derivation of new black hole solutions within the framework of Rastall theory. By decoupling the field equations associated with an extended matter source into two subsystems, we address the first subsystem using the metric components of the regular Bardeen black hole. The second subsystem, incorporating the effects of the additional source, is solved through a constraint imposed by a linear equation of state. By linearly combining the solutions of these subsystems, we obtain two extended models. We then explore the distinct physical properties of these models for specific values of the Rastall and decoupling parameters. Our investigations encompass effective thermodynamic variables such as density and anisotropic pressure, asymptotic flatness, energy conditions, and thermodynamic properties including Hawking temperature, entropy, and specific heat. The results reveal that both models violate asymptotic flatness of the resulting spacetimes. The violation of energy conditions indicate the

*msharif.math@pu.edu.pk

†malick.sallah@utg.edu.gm

presence of exotic matter, for both models. Nonetheless, the energy density, radial pressure, as well as the Hawking temperature exhibit acceptable behavior, while the specific heat and Hessian matrix suggest thermodynamic stability.

Keywords: Rastall gravity; Regularity; Thermodynamic stability.

PACS: 04.50.Kd; 04.40.Dg; 04.40.-b.

1 Introduction

The principle of minimal coupling, integral to general relativity (GR), results in a divergence-free energy-momentum tensor ($\nabla_{\nu_1} T_{\nu_2}^{\nu_1} = 0$) within curved spacetime. In contrast, Rastall proposed a more expansive approach by discarding the minimal coupling principle and introducing a nonminimal coupling between matter and geometry instead [1]. Rastall gravity posits that this nonminimal coupling is linearly dependent on the Ricci scalar \mathcal{R} , i.e., $\nabla_{\nu_1} T_{\nu_2}^{\nu_1} \propto \mathcal{R}_{,\nu_2}$. This distinction becomes apparent in high-curvature, dense matter environments, distinguishing it from GR, although it converges to GR in vacuum conditions. Consequently, compact stars, such as neutron stars, serve as prime candidates for testing Rastall gravity, revealing unique characteristics when applied to such dense stellar objects [2]. Despite assertions that Rastall gravity is essentially equivalent to GR [3], this claim has faced criticism and been refuted due to misinterpretations of the matter stress-energy tensor [4]. Numerous studies across thermodynamic, cosmological, and astrophysical domains have demonstrated the non-equivalence of the two theories [5]-[10].

One of the strongest experimental confirmations of black holes comes from images showing the shadow of a black hole, captured by the Event Horizon Telescope Collaboration [11, 12]. Synge [13] is credited with the ground breaking work on the deflection of light by highly gravitational stars. Bardeen [14] determined that the radius of the photon sphere for a Schwarzschild black hole is $3M$. The discovery of black holes underscored the inadequacies of Newtonian physics in explaining gravity and underscored the significant implications of GR. Even without the presence of matter, the Einstein field equations yield complex solutions like black holes, which possess characteristics vastly different from those of a flat Minkowski spacetime. The fascination with black holes arises from the intricate interplay between classical and quantum physics, which is essential for their understanding. Indeed, the

classical solutions to the Einstein field equations disclose both future [15] and past singularities [16]. The interior of black holes poses a conceptual challenge due to the existence of singularities, typically concealed behind an event horizon [17]. A pivotal advancement in black hole physics was Stephen Hawking pioneering work [18], which clarified the radiation emission from black hole event horizons. This remarkable discovery transformed black holes into crucial experimental sites, providing a unique laboratory for investigating the complex aspects of gravitational theories.

The renowned singularity theorem by Penrose [15] asserts that under specific conditions, singularities are unavoidable in GR. This aligns with the fact that the earliest known exact black hole solutions in GR, feature a singularity within the event horizon. Despite this, it is widely believed that singularities are not physical entities but are instead artifacts produced by classical gravitational theories, and they do not actually exist in nature. Quantum arguments proposed by Sakharov [19] and Gliner [20] suggest that spacetime singularities could be circumvented by matter sources with a de Sitter core at the center of the spacetime. Building on this concept, Bardeen introduced the first static spherically symmetric regular black hole solution [21]. This model was inspired by the Reissner-Nordstrom spacetime. It describes a standard black hole that adheres to the weak energy condition, significantly influencing the trajectory of studies regarding the presence or prevention of singularities. Subsequent models of regular black holes which demonstrate violations of the strong energy condition have since been proposed [22]-[27], thereby challenging the singularity theorems. Ayon-Beato and Garcia [28] established that these models could be viewed as the gravitational fields of nonlinear electric or magnetic monopoles, suggesting that nonlinear electromagnetic fields might be the physical sources of regular black holes. This interpretation is supported by other researchers in the field as well [29].

Exploring the thermodynamic characteristics of black holes is essential for advancing our knowledge of fundamental physics. These characteristics, including temperature, entropy, and specific heat, serve as a bridge connecting quantum mechanics, GR, and statistical mechanics. Investigating how black holes interact with radiation provides researchers with valuable insights into the nature of spacetime, the behavior of quantum fields in intense gravitational environments, and the underlying principles that dictate the universe ultimate fate. This interdisciplinary approach not only enhances our understanding of black holes but also offers a deeper grasp of the fundamental laws of physics under extreme conditions. Bekenstein [30] first linked black hole

surface area to entropy, and subsequently, Hawking [18] showed that black holes with surface gravity (denoted as k) radiate at a temperature of $(\frac{k}{2\pi})$. However, the Bekenstein-Hawking radiation introduces the information loss paradox due to thermal evaporation. To tackle this paradox, Hawking and colleagues [31] recently proposed the concept of soft hair. Owing to the pivotal contributions of Bekenstein and Hawking to black hole thermodynamics, black hole radiation has garnered significant interest from researchers. Recently, there has been a notable increase in the study of black holes and their thermodynamic properties within the context of Rastall gravity theory [32]-[36].

As is well known, solving the Einstein field equations is particularly challenging, especially in scenarios involving spherical symmetry. A recent breakthrough that addresses this complexity is the introduction of a new method called gravitational decoupling via the minimal geometric deformation (MGD) scheme [37]. It later developed into a gravitational source decoupling scheme, enabling the extension of isotropic spherical solutions of the Einstein field equations to anisotropic contexts [38]. Over time, this method has gained widespread acceptance across various modified theories of gravity [39]-[44] including the Rastall theory [45]-[47], significantly contributing to the development of new solutions for the Einstein equations and their extensions. The MGD and the extended geometric deformation (EGD) are the two techniques that comprise the gravitational decoupling scheme. The main difference is that MGD adjusts only the radial part of the spacetime metric, whereas EGD changes both the temporal and radial components. Additionally, MGD is limited to situations where decoupled sources interact solely through gravity, and it cannot be applied to cases with energy exchange between sources. It is worthy to mention, however, that these deformation schemes do not alter the spherical symmetry of the spacetime configuration.

In this study, we profit from the MGD scheme to generalize the regular Bardeen black hole in the context of Rastall theory. We thus obtain new extended solutions, which are analyzed and compared with existing results. The outline of this paper is as follows. In Section **2**, we present the Rastall field equations for a dual matter source and apply the MGD scheme to these equations. Section **3** pertains to the derivation and analysis of two extended solutions, with emphasis on such physical features as asymptotic flatness, and energy conditions. Section **4** entails a thermodynamic analysis of the generalized solutions obtained. Finally, we summarize and analyze our results in Section **5**.

2 Rastall Field Equations

In the context of curved spacetime, Rastall theory [1] diverges from the conventional approach by rejecting the idea of a divergence-free stress-energy tensor, i.e., $\nabla_\nu T^{\nu\omega} \neq 0$. This theory introduces a non-minimal interaction between geometry and matter, achieved by allowing the stress-energy tensor to have a non-zero divergence, i.e.,

$$\nabla^\omega T_{\nu\omega}^R = \frac{\xi}{4} g_{\nu\omega} \nabla^\omega \mathcal{R}, \quad (1)$$

where ξ and \mathcal{R} denote the Rastall parameter and Ricci scalar, respectively. Thus by this equation, Rastall posited that the covariant divergence of the stress-energy tensor is proportional to the divergence of the curvature scalar, \mathcal{R} , with the Rastall parameter as the proportionality constant. Clearly, the usual conservation result of GR is regained in the event $\xi \mapsto 0$ or $\mathcal{R} \mapsto 0$ (flat spacetime). The degree of deviation of the Rastall theory from GR is thus specified by the Rastall parameter, which encapsulates the nature of the non-minimal coupling between geometry and matter. The stress-energy tensor defined in Eq.(1) satisfies the Rastall field equations [3]

$$\mathcal{R}_{\nu\omega} - \frac{1}{2} \mathcal{R} g_{\nu\omega} + \frac{\xi}{4} \mathcal{R} g_{\nu\omega} = \kappa T_{\nu\omega}^R, \quad (2)$$

where $\mathcal{R}_{\nu\omega}$, $g_{\nu\omega}$, and κ denote the Ricci tensor, metric tensor and coupling constant, respectively. Again, we observe that these field equations reduce to the field equations of GR in the event the Rastall parameter vanishes (i.e., $\xi \mapsto 0$). The field equations (2) can be rewritten as

$$\mathcal{R}_{\nu\omega} - \frac{1}{2} \mathcal{R} g_{\nu\omega} = \kappa \hat{T}_{\nu\omega}, \quad (3)$$

where

$$\hat{T}_{\nu\omega} = T_{\nu\omega}^R - \frac{\xi}{4(\xi - 1)} T^R g_{\nu\omega}. \quad (4)$$

From Eq.(4) above, we obtain the following explicit expression for the Rastall stress-energy tensor

$$T_{\nu\omega}^R = \hat{T}_{\nu\omega} - \frac{\xi}{4} \hat{T} g_{\nu\omega}, \quad (5)$$

where

$$\hat{T}_{\nu\omega} = (\rho + P_t) V_\nu V_\omega - P_t g_{\nu\omega} + (P_t - P_r) Y_\nu Y_\omega, \quad (6)$$

is identified as the anisotropic energy-momentum tensor, and \hat{T} as its trace. Here, $V_v = (\sqrt{g_{00}}, 0, 0, 0)$ and $Y_v = (0, -\sqrt{-g_{11}}, 0, 0)$ denote the 4-vector and 4-velocity, respectively, and satisfy the relations

$$V^v Y_v = 0, \quad V^v V_v = 1, \quad Y^v Y_v = -1.$$

As we seek to extend the regular Bardeen black hole solution in this study, we consider a modification of the field equations (1) wherein an extra matter source is gravitationally coupled to the seed source which is specified by the metric potentials of the aforementioned solution. The modified field equations are thus given by

$$\mathcal{R}_{v\omega} - \frac{1}{2}\mathcal{R}g_{v\omega} + \frac{\xi}{4}\mathcal{R}g_{v\omega} = \kappa T_{v\omega}^{(Tot)}, \quad (7)$$

where

$$T_{v\omega}^{(Tot)} = T_{v\omega}^R + \sigma\chi_{v\omega}, \quad (8)$$

and $T_{v\omega}^R$ is given by Eq.(5). In this context, $\chi_{v\omega}$ represents a supplementary source gravitationally linked to the primary source $T_{v\omega}^R$ through the decoupling parameter σ . This supplementary source induces anisotropies within self-gravitating structures and may introduce new fields defined by vectors, tensors, and scalars. The geometry of the spacetime is described by the metric

$$ds^2 = e^{\eta_1(r)} dt^2 - e^{\eta_2(r)} dr^2 - r^2(d\theta^2 + \sin^2\theta d\phi^2). \quad (9)$$

With this metric, the field equations (7) become

$$\begin{aligned} \kappa \left[\rho - \frac{\xi}{4}(\rho - P_r - 2P_t) + \sigma\chi_0^0 \right] &= \frac{1}{r^2} + e^{-\eta_2} \left(\frac{\eta_2'}{r} - \frac{1}{r^2} \right) + \frac{\xi e^{-\eta_2}}{4} \left(\eta_1'' + \frac{\eta_1'(\eta_1' - \eta_2')}{2} \right) \\ &+ \frac{\xi e^{-\eta_2}}{4} \left(\frac{2(\eta_1' - \eta_2')}{r} + \frac{2}{r^2} \right) - \frac{\xi}{2r^2}, \end{aligned} \quad (10)$$

$$\begin{aligned} \kappa \left[P_r + \frac{\xi}{4}(\rho - P_r - 2P_t) - \sigma\chi_1^1 \right] &= -\frac{1}{r^2} + e^{-\eta_2} \left(\frac{\eta_1'}{r} + \frac{1}{r^2} \right) - \frac{\xi e^{-\eta_2}}{4} \left(\eta_1'' + \frac{\eta_1'(\eta_1' - \eta_2')}{2} \right) \\ &- \frac{\xi e^{-\eta_2}}{4} \left(\frac{2(\eta_1' - \eta_2')}{r} + \frac{2}{r^2} \right) + \frac{\xi}{2r^2}, \end{aligned} \quad (11)$$

$$\kappa \left[P_t + \frac{\xi}{4}(\rho - P_r - 2P_t) - \sigma\chi_2^2 \right] = e^{-\eta_2} \left(\frac{\eta_1''}{2} + \frac{\eta_1'^2}{4} - \frac{\eta_1'\eta_2'}{4} + \frac{\eta_1'}{2r} - \frac{\eta_2'}{2r} \right) + \frac{\xi}{2r^2}$$

$$-\frac{\xi e^{-\eta_2}}{4} \left(\eta_1'' + \frac{\eta_1'(\eta_1' - \eta_2')}{2} + \frac{2(\eta_1' - \eta_2')}{r} + \frac{2}{r^2} \right). \quad (12)$$

With respect to this system, the total energy-momentum tensor defined in Eq.(8) is conserved as

$$\nabla^\omega T_{\nu\omega}^{(Tot)} = \frac{dP_r}{dr} + \frac{\eta_1'}{2}(\rho + P_r) + \sigma \frac{\eta_1'}{2}(\chi_1^1 - \chi_0^0) + \frac{2}{r}(P_r - P_t) + \sigma \frac{d\chi_1^1}{dr} + \frac{2\sigma}{r}(\chi_1^1 - \chi_2^2) = 0. \quad (13)$$

The system of equations (10)-(12) constitutes three non-linear ordinary differential equations in eight unknowns, given by ρ , P_r , P_t , η_1 , η_2 , χ_0^0 , χ_1^1 , χ_2^2 . Additionally, the prime notation denotes differentiation with respect to r . From this system, we infer the following effective variables

$$\tilde{\rho} = \rho + \sigma\chi_0^0, \quad \tilde{P}_r = P_r - \sigma\chi_1^1, \quad \tilde{P}_t = P_t - \sigma\chi_2^2. \quad (14)$$

These effective variables prompt an anisotropy defined as

$$F = \tilde{P}_t - \tilde{P}_r = (P_t - P_r) + \sigma(\chi_1^1 - \chi_2^2). \quad (15)$$

In what follows, we exploit the gravitational decoupling technique via the MGD scheme to decouple the field equations (10)-(12). The decoupling process splits the field equations into two sets, the first of which corresponds to the seed source and will be specified by the metric components of the regular Bardeen black hole solution [21]. The second set describes the effects of the extra source and will be solved by employing appropriate constraints. Using Eq.(14), we obtain a linear combination of the solutions of the subfield equations, constituting a solution of the system of the field equations (10)-(12).

3 A Gravitational Decoupling Scheme

The field equations become increasingly complex with the addition of a second source to the original anisotropic fluid, introducing more unknown variables. To achieve an exact solution, it is necessary to limit the degrees of freedom and choose a specific strategy or set of constraints. Thus, we employ a systematic technique known as gravitational decoupling, which when applied to the field equations, allows for the derivation of a solution. A fascinating feature of this technique is that it transforms the temporal-radial

metric potentials into a new reference frame, thereby simplifying the equations. However, we proceed with the MGD scheme of gravitational decoupling wherein only the radial component of the metric is altered. This implies that the temporal metric component is preserved under the MGD scheme. To proceed, we set the coupling parameter σ to zero and examine an anisotropic solution $(\eta_3, \eta_4, \rho, P_r, P_t)$ of the field equations (10)-(12), described by the metric

$$ds^2 = e^{\eta_3(r)} dt^2 - \frac{1}{\eta_4(r)} dr^2 - r^2(d\theta^2 + \sin^2 \theta d\phi^2), \quad (16)$$

where

$$\eta_4(r) = 1 - \frac{2m(r)}{r}, \quad (17)$$

with m denoting the Misner-Sharp mass function.

The geometric deformation on the metric functions are applied through the following linear transformations

$$\eta_3(r) \mapsto \eta_1(r) = \eta_3(r) + \sigma f(r), \quad \eta_4(r) \mapsto e^{-\eta_2(r)} = \eta_4(r) + \sigma h(r), \quad (18)$$

with $f(r)$ and $h(r)$ as the deformations on g_{tt} and g_{rr} , respectively. Owing to the MGD scheme, we set $f(r) = 0$, implying that the temporal component of the metric is preserved. Substituting these transformations into the field equations, we obtain two sets of subfield equations. The first of these corresponds to $\sigma = 0$ and is given by

$$\begin{aligned} \kappa \left[\rho - \frac{\xi}{4}(\rho - P_r - 2P_t) \right] &= \eta_4 \left(\frac{\xi \eta_3''}{4} - \frac{1}{r^2} + \frac{\xi \eta_3'^2}{8} + \frac{\xi \eta_3'}{2r} + \frac{\xi}{2r^2} \right) \\ &+ \eta_4' \left(\frac{\xi}{2r} + \frac{\xi \eta_3'}{8} - \frac{1}{r} \right) - \frac{\xi}{2r^2} + \frac{1}{r^2}, \end{aligned} \quad (19)$$

$$\begin{aligned} \kappa \left[P_r + \frac{\xi}{4}(\rho - P_r - 2P_t) \right] &= \eta_4 \left(\frac{\eta_3'}{r} - \frac{\xi \eta_3''}{4} + \frac{1}{r^2} - \frac{\xi \eta_3'^2}{8} - \frac{\xi \eta_3'}{2r} - \frac{\xi}{2r^2} \right) \\ &- \eta_4' \left(\frac{\xi \eta_3'}{8} + \frac{\xi}{2r} \right) + \frac{\xi}{2r^2} - \frac{1}{r^2}, \end{aligned} \quad (20)$$

$$\begin{aligned} \kappa \left[P_t + \frac{\xi}{4}(\rho - P_r - 2P_t) \right] &= \eta_4 \left(\frac{\eta_3''}{2} + \frac{\eta_3'^2}{4} + \frac{\eta_3'}{2r} - \frac{\xi \eta_3''}{4} - \frac{\xi \eta_3'^2}{8} - \frac{\xi \eta_3'}{2r} - \frac{\xi}{2r^2} \right) \\ &+ \eta_4' \left(\frac{\eta_3'}{4} + \frac{1}{2r} - \frac{\xi \eta_3'}{8} - \frac{\xi}{2r} \right) + \frac{\xi}{2r^2}. \end{aligned} \quad (21)$$

The conservation equation with respect to this set becomes

$$\frac{dP_r}{dr} + \frac{\eta'_3}{2}(\rho + P_r) + \frac{2}{r}(P_r - P_t) = 0. \quad (22)$$

It can be observed that the system (19)-(21), consists of three equations in the five variables $(\rho, P_r, P_t, \eta_3, \eta_4)$. It therefore suffices to adopt two constraints to close this system. For this, we shall employ the metric potentials of the regular Bardeen black hole [21].

The second set incorporates the effects of the extra source $\chi_{\nu\omega}$, and is obtained by turning on the effect of the decoupling parameter σ . This set is given by the system

$$\kappa\chi_0^0 = h\left(\frac{\xi}{2r^2} + \frac{\xi\eta'_3}{2r} + \frac{\xi\eta_3'^2}{8} + \frac{\xi\eta_3''}{4} - \frac{1}{r^2}\right) + h'\left(\frac{\xi}{2r} + \frac{\xi\eta'_3}{8} - \frac{1}{r}\right), \quad (23)$$

$$\kappa\chi_1^1 = h\left(\frac{\xi}{2r^2} + \frac{\xi\eta'_3}{2r} + \frac{\xi\eta_3'^2}{8} + \frac{\xi\eta_3''}{4} - \frac{1}{r^2} - \frac{\eta'_3}{r}\right) + h'\left(\frac{\xi}{2r} + \frac{\xi\eta'_3}{8}\right), \quad (24)$$

$$\begin{aligned} \kappa\chi_2^2 = & h\left(\frac{\xi}{2r^2} + \frac{\xi\eta'_3}{2r} + \frac{\xi\eta_3'^2}{8} + \frac{\xi\eta_3''}{4} - \frac{\eta'_3}{2r} - \frac{\eta_3'^2}{4} - \frac{\eta_3''}{2}\right) \\ & + h'\left(\frac{\xi}{2r} + \frac{\xi\eta'_3}{8} - \frac{1}{2r} - \frac{\eta'_3}{4}\right). \end{aligned} \quad (25)$$

This system is conserved according to the equation below

$$\frac{d\chi_1^1}{dr} + \frac{\eta'_3}{2}(\chi_1^1 - \chi_0^0) + \frac{2}{r}(\chi_1^1 - \chi_0^0) = 0. \quad (26)$$

It is observed that this system comprises three equations in four variables, viz $(\chi_0^0, \chi_1^1, \chi_2^2, h)$. A single constraint is thus sufficient to close this system. It is worthy to highlight that the subfield equations (19)-(21) and (23)-(25) are each individually conserved. This implies that there is a null exchange of energy momentum between the sources, which is a necessary condition for the applicability of the MGD scheme.

4 Extending the Regular Bardeen Black Hole Solution

The regular Bardeen black hole solution is described by the line element [21]

$$ds^2 = \left(1 - \frac{2Mr^2}{(r^2 + e^2)^{\frac{3}{2}}}\right) dt^2 - \left(1 - \frac{2Mr^2}{(r^2 + e^2)^{\frac{3}{2}}}\right)^{-1} dr^2 - r^2(d\theta^2 + \sin^2\theta d\phi^2), \quad (27)$$

where M and e denote the mass and magnetic monopole charge of the black hole, respectively. The metric above has a coinciding Killing (r_H) and causal horizons (r_h) at the surface. The coincidence of the Killing and causal horizons is a necessary condition for the deformed Bardeen metric (29) to denote a proper black hole. These horizons are specified by the conditions $e^{\eta_1} = 0$ and $e^{-\eta_2} = 0$, respectively [48]. The Killing horizon for the regular Bardeen black hole metric is thus obtained as

$$r_H = \sqrt{Ae^2 + \frac{B+C}{3} + \frac{4M^2}{3}}, \quad (28)$$

where

$$A = -\frac{2^{8/3}M^2}{\sqrt[3]{27e^4M^2 - 72e^2M^4 + 3\sqrt{81e^8M^4 - 48e^6M^6} + 32M^6}} - 1,$$

$$B = \frac{2^{11/3}M^4}{\sqrt[3]{27e^4M^2 - 72e^2M^4 + 3\sqrt{81e^8M^4 - 48e^6M^6} + 32M^6}},$$

$$C = \sqrt[3]{54e^4M^2 - 144e^2M^4 + 6\sqrt{81e^8M^4 - 48e^6M^6} + 64M^6}.$$

Using the minimal deformation of the metric (27), we obtain extensions of the regular Bardeen black hole solution. The line element for the minimally deformed Bardeen black hole solution is given by

$$ds^2 = \left(1 - \frac{2Mr^2}{(r^2 + e^2)^{\frac{3}{2}}}\right) dt^2 - \left(1 - \frac{2Mr^2}{(r^2 + e^2)^{\frac{3}{2}}} + \sigma h(r)\right)^{-1} dr^2 - r^2(d\theta^2 + \sin^2\theta d\phi^2), \quad (29)$$

where $h(r)$ is obtained from the system (23)-(25), by specifying a constraint on the extra source, $\chi_{\nu\omega}$. These constraints are specified by the linear equation of state (EoS) [48]

$$\chi_0^0 + \lambda\chi_1^1 + \tau\chi_2^2 = 0, \quad (30)$$

where λ and τ are real constants.

In what follows, we obtain two extensions of the regular Bardeen black hole solution, using two specific cases of the EoS mentioned above (30).

4.1 Model I: Traceless Additional Source

The additional source $\chi_{\nu\omega}$ is termed as conformally symmetric when its energy-momentum tensor possesses a null trace. As $\chi_2^2 = \chi_3^3$ (due to the spherical symmetry), a traceless additional source is implied if

$$\chi_0^0 + \chi_1^1 + 2\chi_2^2 = 0, \quad (31)$$

i.e., when $\lambda = 1$ and $\tau = 2$ in (30). Using the system (23)-(25), Eq.(31) above simplifies to

$$\frac{(\xi - 1) (rh'(r) (r\eta_3'(r) + 4) + h(r) (2r^2\eta_3''(r) + (r\eta_3'(r) + 2)^2))}{2r^2} = 0, \quad (32)$$

from which $h(r)$ can be obtained. Due to a complicated expression, the result for $h(r)$ from (32) is not written. Nonetheless, its graph is shown in Figure 1. We would like to mention here that for all the plots, we have used values of the Rastall and decoupling parameters as $\xi = 0.2, 0.6$ and $\sigma = 0.2, 0.4, 0.6, 0.8, 1$, respectively, while the magnetic monopole charge has been fixed at $e = 1$. Additionally, we have used $M = 1$, in order to cater for a region accessible to an outer observer. Substituting the deformation function obtained from Eq.(32) above into the deformed Bardeen metric (29), we obtain an extended solution. This extended model is described by the following effective variables

$$\begin{aligned} \tilde{\rho} &= \frac{3e^2 M (4e^2(\xi - 1) - (\xi + 4)r^2)}{16\pi(\xi - 1) (e^2 + r^2)^{7/2}} + \sigma\chi_0^0, \\ \tilde{P}_r &= \frac{3e^2 M ((\xi + 4)r^2 - 4e^2(\xi - 1))}{16\pi(\xi - 1) (e^2 + r^2)^{7/2}} - \sigma\chi_1^1, \\ \tilde{P}_t &= -\frac{3e^2 M (4e^2(\xi - 1) + (6 - 11\xi)r^2)}{16\pi(\xi - 1) (e^2 + r^2)^{7/2}} - \sigma\chi_2^2. \end{aligned} \quad (33)$$

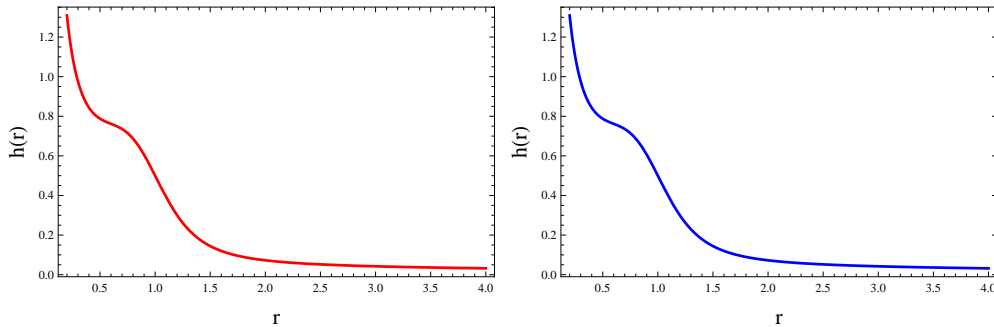


Figure 1: Graphs of deformation function $h(r)$ against r with $\xi = 0.2$ (left), 0.6 (right) for model I.

It is fundamental to investigate whether the extended model preserves the regularity of the Bardeen black hole. It is observed that the inclusion of the deformation function $h(r)$ creates the divergence of the extended models (29), from the standard Bardeen black hole (27). This implies that the extended model is regular if the associated deformation function is nonsingular at the core. Figure 1 shows that the deformation function obtained for the first model is regular at the core, thus implying the regularity of the associated extended model. We additionally provide a graph of the modified metric coefficient, enabling us to evaluate the asymptotic flatness of the new spacetime. If the metric potentials of a spacetime converge to 1 as the radial distance increases arbitrarily, the spacetime is said to be asymptotically flat. The gravitational field gradually decreases in such a spacetime and vanishes completely at great distances from a huge entity. This suggests that spacetime seems flat at large distances, much like the flat spacetime that special relativity describes, when gravity is essentially nonexistent.

Figure 2 portrays that the criteria for asymptotic flatness has been violated by the radial metric component. It should be noted that we only employed the graphical analysis for the deformed radial metric component of the extended solution in our analysis of the asymptotic flatness. This is because it is readily inferred from the deformed metric (29), that $\lim_{r \rightarrow \infty} g_{tt} = 1$. The effective parameters (33) are plotted in Figure 3. We observe a positive density and negative radial pressure, which is the acceptable behavior for these parameters. A negative radial pressure implies an inward force that amplifies the gravitational pull of a black hole. This idea fits well with the

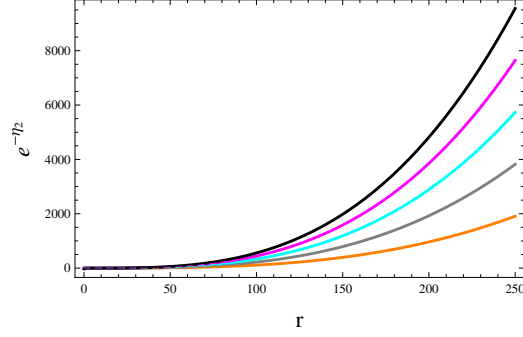


Figure 2: Graph of $e^{-\eta_2}$ against r with $\xi = 0.2$ (solid), 0.6 (dashed), $\sigma = 0.2$ (orange), 0.4 (gray), 0.6 (cyan), 0.8 (magenta) and 1 (black) for model I.

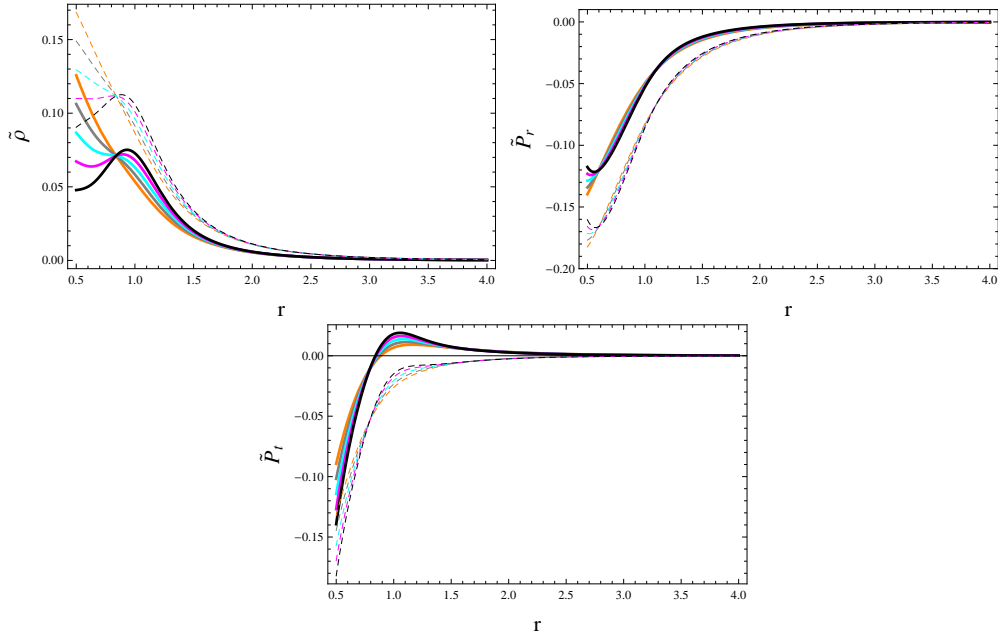


Figure 3: Graphs of effective parameters against r with $\xi = 0.2$ (solid), 0.6 (dashed), $\sigma = 0.2$ (orange), 0.4 (gray), 0.6 (cyan), 0.8 (magenta) and 1 (black) for model I.

current understanding, where matter collapses into a singularity due to immense gravitational forces. In theoretical models, negative radial pressure frequently aids in explaining various phenomena, such as the accelerated expansion of the universe, as observed in theories involving dark energy with negative pressure. Additionally, the energy density and radial pressure exhibit a direct and indirect variance, respectively, to the Rastall parameter ξ . The tangential pressure however, assumes both negative and positive values in its domain whilst varying inversely with the Rastall parameter. With respect to the decoupling parameter σ , the effective parameters exhibit a discrepancy as they vary both directly and indirectly in different intervals within their domains.

To ascertain the characteristics of the matter source, $T_{\nu\omega}^{(Tot)}$, we additionally plot the energy conditions. The energy-momentum tensor of the source is constrained by these energy conditions, which comprise dominant, strong, null, and weak classifications. The source is regarded as normal if the energy criteria are met, and exotic if certain energy requirements are not met. The classification of these energy conditions are given as follows

- Dominant Energy Conditions
 $\tilde{\rho} \geq |\tilde{P}_r|, \quad \tilde{\rho} \geq |\tilde{P}_t|.$
- Strong Energy Conditions
 $\tilde{\rho} \geq -\tilde{P}_r, \quad \tilde{\rho} \geq -\tilde{P}_t, \quad \tilde{\rho} + \tilde{P}_r \geq -2\tilde{P}_t.$
- Null Energy Conditions
 $\tilde{\rho} \geq -\tilde{P}_r, \quad \tilde{\rho} \geq -\tilde{P}_t.$
- Weak Energy Conditions
 $\tilde{\rho} \geq 0, \quad \tilde{\rho} \geq -\tilde{P}_r, \quad \tilde{\rho} \geq -\tilde{P}_t.$

These graphs of the energy conditions plotted in Figure 4, depict that the matter source $T_{\nu\omega}^{(Tot)}$ is exotic.

4.2 Model II: A Barotropic EoS

A barotropic EoS is a unique case of a polytropic EoS. The additional source $\chi_{\nu\omega}$ describes a barotropic fluid if it satisfies the EoS

$$\delta(\chi_0^0) - \chi_1^1 = 0, \tag{34}$$

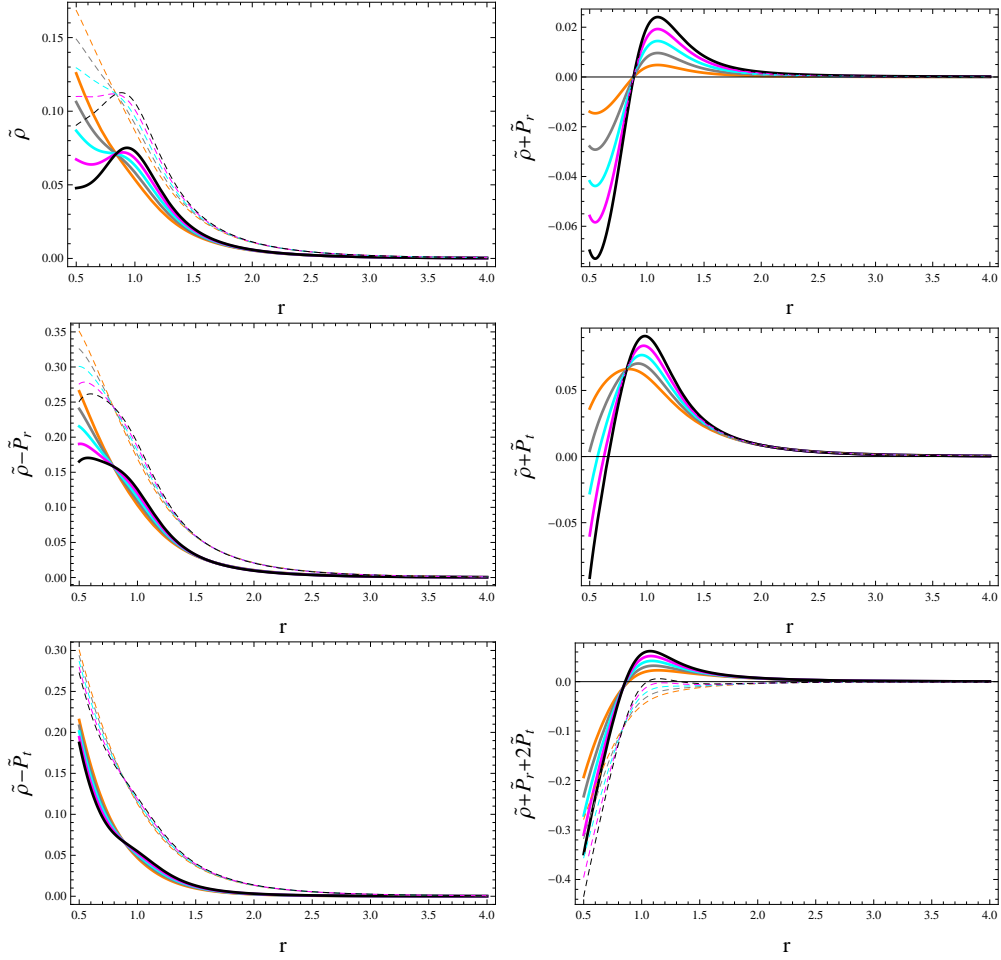


Figure 4: Graphs of energy conditions against r with $\xi = 0.2$ (solid), 0.6 (dashed), $\sigma = 0.2$ (orange), 0.4 (gray), 0.6 (cyan), 0.8 (magenta) and 1 (black) for model I.

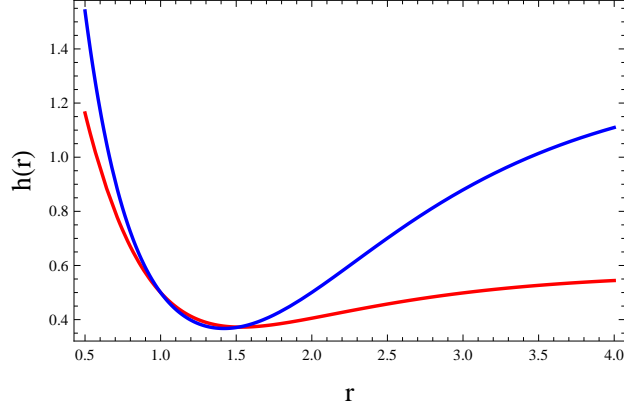


Figure 5: Graphs of deformation function $h(r)$ against r with $\xi = 0.2$ (red), 0.6 (blue) for model II.

where δ denotes a nonnegative parameter which incorporates information about the temperature. It can be observed that this equation is a special case of the linear EoS (30) with $\lambda = -\frac{1}{\delta}$ and $\tau = 0$. Using the system (23)-(25), the barotropic EoS (34) becomes

$$\begin{aligned} & \frac{rh'(r)(\delta + 1)\xi r\eta_3'(r)}{8r^2} + \frac{rh(r)\eta_3'(r)((\delta - 1)\xi r\eta_3'(r) + 4(\delta - 1)\xi + 8)}{8r^2} \\ & + \frac{4(\delta(\xi - 2) + \xi)}{8r^2} + \frac{rh(r)2(\delta - 1)\xi r\eta_3''(r)}{8r^2} + \frac{4h(r)(\delta - 1)(\xi - 2)}{8r^2} = 0, \end{aligned} \quad (35)$$

from which we obtain the deformation function $h(r)$. Due to the complexity and length of the expression, the explicit form of $h(r)$ is omitted. Instead, its graph is shown below. By substituting this deformation function into the minimally deformed Bardeen metric from Eq.(29), we derive another extended solution. This new model is defined by the effective parameters outlined in Eq.(33). The distinction here is that the deformation function used is derived from Eq.(35). The deformation function in Figure 5 indicates the absence of singularities within its domain. Consequently, by the same reasoning as in the prior section, it can be inferred that the extended model created with this deformation function maintains the regularity of the Bardeen metric as given in Eq.(27). Figure 6 shows that the resulting spacetime lacks asymptotic flatness.

The effective variables in Figure 7 provide further insights into the de-

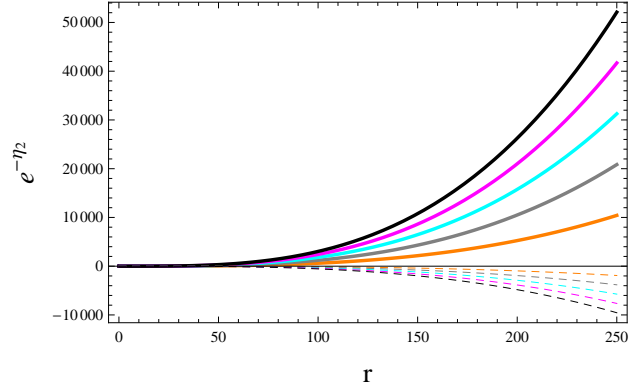


Figure 6: Graph of $e^{-\eta_2}$ against r with $\xi = 0.2$ (solid), 0.6 (dashed), $\sigma = 0.2$ (orange), 0.4 (gray), 0.6 (cyan), 0.8 (magenta) and 1 (black) for model II.

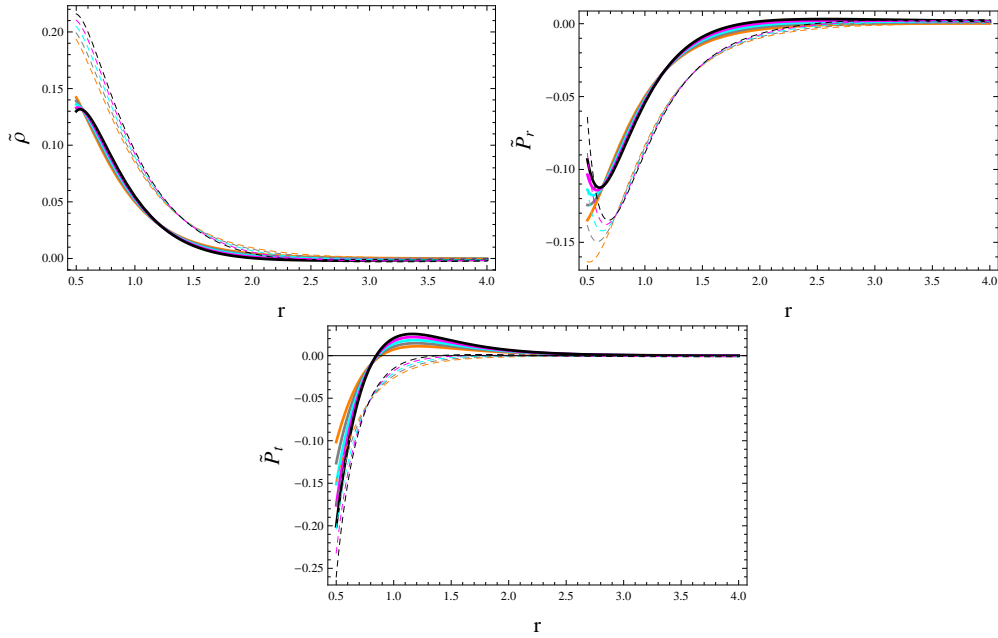


Figure 7: Graphs of effective parameters against r with $\xi = 0.2$ (solid), 0.6 (dashed), $\sigma = 0.2$ (orange), 0.4 (gray), 0.6 (cyan), 0.8 (magenta) and 1 (black) for model II.

rived model. Similar to the model discussed in the previous section, this model features a positive density and a negative radial pressure, while the tangential pressure alternates between negative and positive values. With respect to the Rastall parameter, the density varies directly, while the radial and tangential pressures vary inversely. Regarding the decoupling parameter σ , the effective parameters show a diverging variation as they vary both directly and indirectly across various intervals within their domains. Finally, we plot the energy conditions in Figure 8 where a violation of some energy conditions indicate an exotic source.

5 Some Thermodynamic Properties

In this part, we explore various thermodynamic properties of black holes. Factors such as temperature, entropy, and specific heat, connect quantum mechanics, GR, and statistical mechanics. Studying the radiation absorption and emission by black holes helps scientists to discover details about the nature of spacetime, the behavior of quantum fields in strong gravitational environments, and the fundamental principles governing the fate of the universe. This interdisciplinary approach not only deepens our comprehension of black holes but also enhances our knowledge of the most extreme physical laws.

5.1 Hawking Radiation Temperature

The temperature associated with Hawking radiation, often referred to as Hawking temperature T_H , is a crucial thermodynamic characteristic of black holes that provides significant insights into the interplay between quantum mechanics and gravity. This phenomenon, predicted by Stephen Hawking [18], involves the emission of radiation from black holes as a result of quantum effects occurring near the event horizon. This radiation temperature is inversely related to the mass of the black hole, meaning that smaller black holes emit more radiation and have higher temperatures. This discovery not only challenges the traditional view of black holes as entities that only absorb matter but also indicates that they can gradually lose mass and energy, potentially leading to their complete evaporation. Investigating Hawking temperature offers a distinctive perspective on the quantum properties of black holes, linking theoretical models with observable cosmic events. The

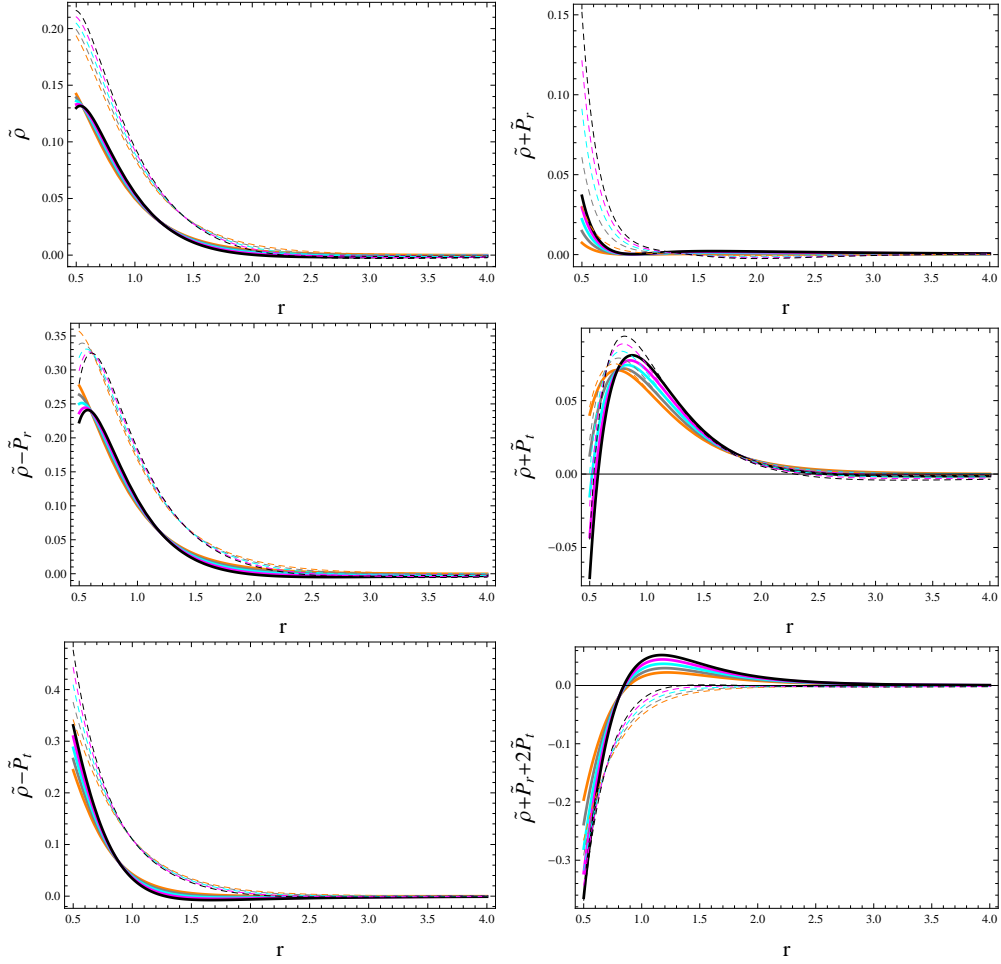


Figure 8: Graphs of effective parameters against r with $\xi = 0.2$ (solid), 0.6 (dashed), $\sigma = 0.2$ (orange), 0.4 (gray), 0.6 (cyan), 0.8 (magenta) and 1 (black) for model II.

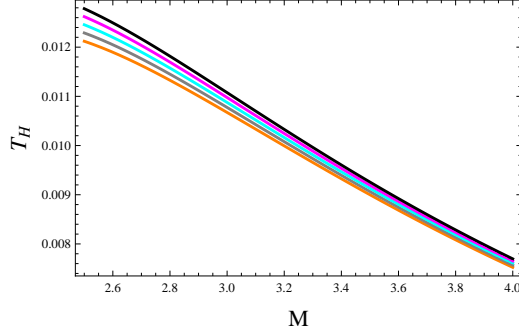


Figure 9: Graph of T_H against M with $\xi = 0.2$ (solid), 0.6 (dashed), $\sigma = 0.2$ (orange), 0.4 (gray), 0.6 (cyan), 0.8 (magenta) and 1 (black) for model I.

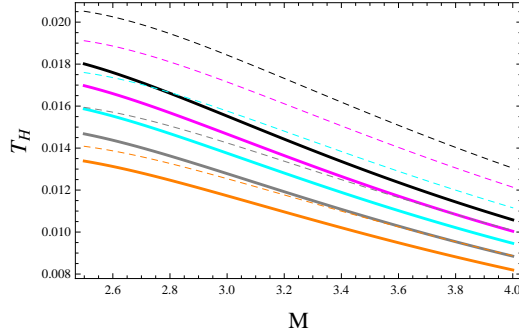


Figure 10: Graph of T_H against M with $\xi = 0.2$ (solid), 0.6 (dashed), $\sigma = 0.2$ (orange), 0.4 (gray), 0.6 (cyan), 0.8 (magenta) and 1 (black) for model II.

expression for the Hawking temperature is

$$T_H = \frac{k}{2\pi} = \frac{1}{4\pi} \left| \frac{g_{tt,r}}{\sqrt{-g_{tt}g_{rr}}} \right|_{r=r_H}. \quad (36)$$

The Hawking temperature for model I in Figure 9 demonstrates appropriate behavior, indicating an inverse relationship between temperature and black hole mass. However, variations in the Rastall parameter show a negligible effect on the Hawking temperature, whereas the decoupling parameter shows a direct correlation. Similarly, the Hawking temperature for model II (Figure 10) exhibits acceptable behavior. In this case, contrary to model I, the Rastall parameter has a noticeable impact, directly influencing the Hawking temperature, alongside the decoupling parameter.

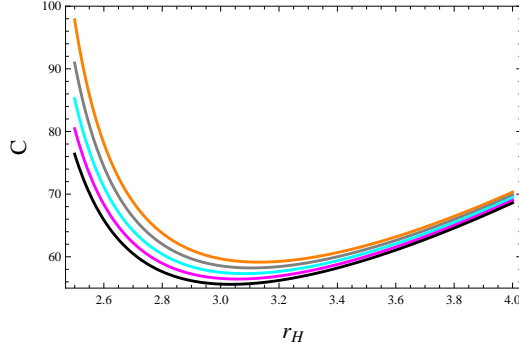


Figure 11: Graph of C against r_H with $\xi = 0.2$ (solid), 0.6 (dashed), $\sigma = 0.2$ (orange), 0.4 (gray), 0.6 (cyan), 0.8 (magenta) and 1 (black) for model I.

5.2 Specific Heat

The specific heat is a critical thermodynamic parameter for evaluating the thermal stability of black holes, measuring the amount of heat needed to produce a small temperature change in a black hole. In black hole thermodynamics, specific heat can indicate stability properties. A positive specific heat means the black hole can reach thermal equilibrium with its surroundings, implying stability. Conversely, a negative specific heat signals instability, leading to runaway heating or cooling during heat exchange. This behavior is particularly evident in various black hole models, such as Schwarzschild and Kerr black holes, where variations in specific heat can highlight phase transitions or critical points in their thermodynamic properties.

The expression for the specific heat capacity is given by

$$C = T_H \left(\frac{\partial S}{\partial T_H} \right) \Big|_{r=r_H} = T_H \left(\frac{\partial S}{\partial r_H} \right) \left(\frac{\partial T_H}{\partial r_H} \right)^{-1}, \quad (37)$$

where

$$S = \frac{1}{4} \int_0^{2\pi} \int_0^\pi \sqrt{g_{\theta\theta}g_{\phi\phi}} d\theta d\phi = \pi r_H^2, \quad (38)$$

denotes the Bekenstein-Hawking entropy [49]. Figure **11** shows a positive specific heat for the first model, in the interval $2.5 \leq r_H \leq 4$. This implies that the system is stable in this interval. It is observed that the Rastall parameter shows no variation with respect to the specific heat, while the decoupling parameter varies inversely. For the second model (Figure **12**), we

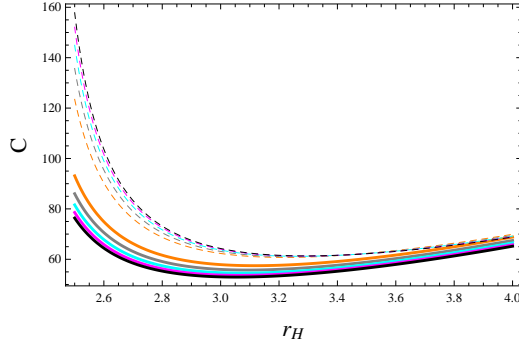


Figure 12: Graph of C against r_H with $\xi = 0.2$ (solid), 0.6 (dashed), $\sigma = 0.2$ (orange), 0.4 (gray), 0.6 (cyan), 0.8 (magenta) and 1 (black) for model II.

observe a direct variation of the specific heat to the Rastall parameter. The decoupling parameter varies inversely to the specific heat, when considered with the lower value of the Rastall parameter ($\xi = 0.2$). The decoupling parameter, however, varies directly with the specific heat corresponding to ($\xi = 0.6$). This model also exhibits stability in the interval $2.5 \leq r_H \leq 4$, as a positive specific heat is registered.

5.3 Hessian Matrix

The Hessian matrix, particularly through its trace, provides valuable insights into the thermodynamic stability of black holes. This matrix comprises second-order partial derivatives of the Helmholtz free energy, $F = E - ST_H$, with E representing internal energy, S representing entropy, and T_H representing the Hawking temperature of the black hole. These derivatives are calculated with respect to temperature and volume, where the temperature is specified by the Hawking temperature and the volume is given by $V = \frac{4}{3}\pi r_H^3$. The Hessian matrix is given by

$$H = \begin{pmatrix} H_{11} & H_{12} \\ H_{21} & H_{22} \end{pmatrix} = \begin{pmatrix} \frac{\partial^2 F}{\partial T_H^2} & \frac{\partial^2 F}{\partial T_H \partial V} \\ \frac{\partial^2 F}{\partial V \partial T_H} & \frac{\partial^2 F}{\partial V^2} \end{pmatrix}. \quad (39)$$

It can be observed that $\det(H) = 0$, which suggests that the given Hessian matrix has an eigenvalue of zero. The positive definiteness of the Hessian matrix cannot thus be exploited to determine the stability of the system.

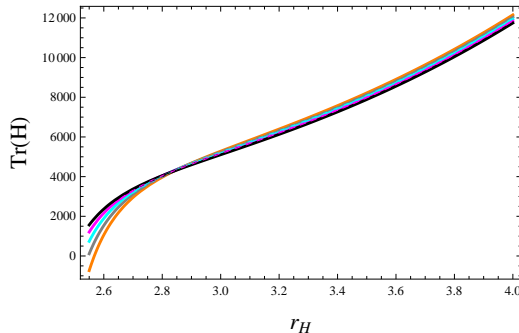


Figure 13: Graph of $Tr(H)$ against r_H with $\xi = 0.2$ (solid), 0.6 (dashed), $\sigma = 0.2$ (orange), 0.4 (gray), 0.6 (cyan), 0.8 (magenta) and 1 (black) for model I.

We therefore determine the stability by using the trace of the Hessian matrix given by

$$Tr(H) = H_{11} + H_{22}. \quad (40)$$

Here, the criterion for stability is that $Tr(H) \geq 0$ [50]. Due to very lengthy and complicated expressions, the explicit form of the trace is not written. However, the plots of the trace versus horizon radius (r_H) are shown for both models.

The graphical analysis of $Tr(H)$ for the first model is shown in Figure **13**, which indicates that the model is stable in the interval $2.575 \leq r_H \leq 4$. However, we observe a null/negligible effect in the fluctuation of the Rastall parameter, while the decoupling parameter shows a direct variation to $Tr(H)$ in the interval $2.575 \leq r_H \leq 2.8$ and inverse variation in the rest of the interval. For the second model (Figure **14**), we deduce that the system is stable in the interval $2.5 < r_H \leq 4$, when considered with the Rastall parameter $\xi = 0.2$. With the Rastall parameter $\xi = 0.6$, the interval of stability becomes $2.65 < r_H \leq 4$. It is thus deduced that for both Rastall parameters used, the system is stable in the interval $2.65 < r_H \leq 4$. Additionally, we observe an overall indirect variation of the Rastall and decoupling parameters to the trace, $Tr(H)$.

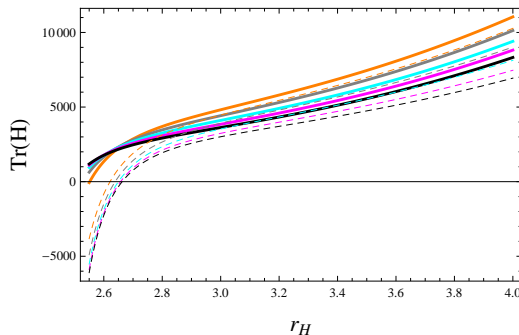


Figure 14: Graph of $Tr(H)$ against r_H with $\xi = 0.2$ (solid), 0.6 (dashed), $\sigma = 0.2$ (orange), 0.4 (gray), 0.6 (cyan), 0.8 (magenta) and 1 (black) for model II.

6 Conclusions

In this study, we have identified minimally decoupled regular Bardeen black hole solutions within the framework of Rastall gravity. We have formulated the field equations and utilized the MGD scheme to optimize the gravitational decoupling process. This method separates the field equations into two distinct sets. The first set corresponds to the regular Bardeen black hole, while the second set involves an additional source, $\chi_{\nu\omega}$, which is gravitationally linked to the primary source through the decoupling parameter, σ . This supplementary source enables the extension of the regular Bardeen black hole, allowing the derivation of new black hole solutions that retain the physical properties of the original Bardeen black hole.

The comprehensive solutions are derived through a linear combination of the solutions to the subfield equations, which are obtained post-decoupling. The solution to the first system is determined by the metric components of the regular Bardeen black hole, whereas the solution to the second system is derived using specific constraints provided by a linear EoS. We have identified two extended solutions corresponding to two particular instances of the given EoS. Our findings indicate that both extended models maintain the regularity of the original Bardeen black hole, aligning with the results in reference [51]. For both models, we have examined the effects of the Rastall and decoupling parameters, ξ and σ , respectively, using the values $\xi = 0.2, 0.6$ and $\sigma = 0.2, 0.4, 0.6, 0.8, 1$.

We have observed a positive energy density paired with a negative radial

pressure for both models. Our investigation into the asymptotic flatness of these models revealed that none of the resulting solutions maintain asymptotic flatness. To analyze asymptotic flatness, we have focused exclusively on the deformed radial metric coefficient, as the temporal metric coefficient, which remains unchanged, evidently approaches to 1 as r becomes arbitrarily large. Additionally, our findings indicate that both models involve exotic matter, as they violate certain energy conditions.

Our investigation into the thermodynamic properties of both models revealed that black holes with lower mass emitted higher levels of radiation. This outcome aligns with theoretical expectations, as the emission of radiation results in evaporation and thus a reduction in mass. Specifically, in the first model, the Rastall parameter demonstrated only a minor fluctuation, whereas the decoupling parameter has shown a direct correlation with the Hawking temperature. Conversely, in the second model, both the Rastall and decoupling parameters have displayed a direct relationship with the Hawking radiation temperature.

We have examined thermodynamic stability of both models by analyzing heat capacity and trace of the Hessian matrix. The heat capacity analysis indicates that both models remain stable within the range $2.5 \leq r_H \leq 4$. In contrast, the Hessian matrix trace analysis reveals stability ranges of $2.575 \leq r_H \leq 4$ for the first model and $2.65 < r_H \leq 4$ for the second model. Consequently, we can conclude that both models exhibit stability within the interval $2.65 < r_H \leq 4$.

Data Availability: No data was used for the research described in this paper.

References

- [1] P. Rastall, Phys. Rev. D 6 (1972) 3357; Can. J. Phys. 54 (1976) 66.
- [2] W. El Hanafy, Astrophys. J. 940 (2022) 51; W. El Hanafy, A. Awad, Astrophys. J. 951 (2023) 144.
- [3] M. Visser, Phys. Lett. B 782 (2018) 83.
- [4] F. Darabi, et al., Eur. Phys. J. C 78 (2018) 25.

- [5] K. Bamba, A. Jawad, S. Rafique, H. Moradpour, *Eur. Phys. J. C* 78 (2018) 986.
- [6] M. Cruz, S. Lepe, G. Morales-Navarrete, *Class. Quantum Grav.* 36 (2019) 225007.
- [7] K. Lin, W.L. Qian, *Eur. Phys. J. C* 80 (2020) 561.
- [8] A.H. Ziaie, H. Moradpour, H. Shabani, *Eur. Phys. J. Plus* 135 (2020) 916.
- [9] Q. Li, et al., *Eur. Phys. J. C* 82 (2022) 658.
- [10] G.G.L. Nashed, W. El Hanafy, *Eur. Phys. J. C* 82 (2022) 679.
- [11] K. Akiyama, et al., *Astrophys. J. Lett.* 875 (2019) L2.
- [12] K. Akiyama, et al., *Astrophys. J. Lett.* 875 (2019) L5; *ibid.* 875 (2019) L6.
- [13] J.L. Synge, *Mon. Not. Roy. Astron. Soc.* 131 (1966) 463.
- [14] J. Bardeen, *Astrophys. J.* 178 (1972) 347.
- [15] R. Penrose, *Phys. Rev. Lett.* 14 (1965) 57.
- [16] S.W. Hawking, *Phys. Rev. Lett.* 15 (1965) 689; *Proc. Roy. Soc. Lond. A* 294 (1966) 511; *ibid.* 295 (1966) 490; *ibid.* 300 (1967) 187.
- [17] W. Israel, *Commun. Math. Phys.* 8 (1968) 245.
- [18] S.W. Hawking, *Nature* 248 (1974) 30; *Commun. Math. Phys.* 43 (1975) 199.
- [19] A.D. Sakharov, *J. Exp. Theor. Phys.* 22 (1966) 241.
- [20] E.B. Gliner, *J. Exp. Theor. Phys.* 22 (1966) 378.
- [21] J. Bardeen, *Proc. GR5, (Tiflis, USSR, 1968).*
- [22] A. Borde, *Phys. Rev. D* 50 (1994) 3692.
- [23] C. Barrabes, V.P. Frolov, *Phys. Rev. D* 53 (1996) 3215.

- [24] A. Bogojevic, D. Stojkovic, Phys. Rev. D 61 (2000) 084011.
- [25] A. Cabo, A.E. Beato, Int. J. Mod. Phys. A 14 (1999) 2013.
- [26] S.A. Hayward, Phys. Rev. Lett. 96 (2006) 031103.
- [27] C. Bambi, L. Modesto, Phys. Lett. B 721 (2013) 329.
- [28] A.E. Beato, A. Garcia, Phys. Rev. Lett. 80(1998)5056; Gen. Relativ. Gravit. 31 (1999) 629; Phys. Lett. B 464 (1999) 25; ibid. 493 (2000) 149; Gen. Relativ. Gravit. 37 (2005) 635.
- [29] M.S. Ma, Ann. Phys. 362 (2015) 529.
- [30] J.D. Bekenstein, Phys. Rev. D 9 (1974) 3292.
- [31] S.W. Hawking, M.J. Perry, A. Strominger, Phys. Rev. Lett. 116 (2016) 231301.
- [32] Y. Heydarzade, H. Moradpour, F. Darabi, Can. J. Phys. 95 (2017) 1253.
- [33] R. Kumar, S.G. Ghosh, Eur. Phys. J. C 78 (2018) 750.
- [34] I.P. Lobo, et al., Int. J. Mod. Phys. D 27 (2018) 1850069.
- [35] H.L. Prihadi, et al., Int. J. Mod. Phys. D 29 (2020) 2050021.
- [36] B. Toshmatov, Z. Stuchlik, B. Ahmedov, Phys. Dark Universe 41 (2023) 101257.
- [37] J. Ovalle, Phys. Rev. D 95 (2017) 104019.
- [38] J. Ovalle, R. Casadio, R. da Rocha, A. Sotomayor, Eur. Phys. J. C 78 (2018) 122.
- [39] M. Sharif, S. Sadiq, Eur. Phys. J. C 78 (2018) 410.
- [40] M. Sharif, S. Naz, Mod. Phys. Lett. A 35 (2020) 1950340.
- [41] M. Sharif, T. Naseer, Chin. J. Phys. 73 (2021) 179.
- [42] T. Naseer, M Sharif, Universe 8 (2022) 62.
- [43] M. Sharif, K. Hassan, Eur. Phys. J. Plus 137 (2022) 997.

- [44] K. Hassan, M. Sharif, *Universe* 9 (2023) 165.
- [45] S.K. Maurya, F. Tello-Ortiz, *Phys. Dark Universe* 29 (2020) 100577.
- [46] S. Sadiq, et al., *Front. Astron. Space Sci.* 10 (2024) 1320081.
- [47] M. Sharif, M. Sallah, *New Astron.* 109 (2024) 102198; *Eur. Phys. J. Plus* 139 (2024) 819.
- [48] J. Ovalle, et al., *Eur. Phys. J. C* 78 (2018) 960.
- [49] G.W. Gibbons, S.W. Hawking, *Phys. Rev. D* 15 (1977) 2752.
- [50] B. Cuadros-Melgar, et al., *Eur. Phys. J. C* 80 (2020) 848.
- [51] M. Misyura, A. Rincon, V. Vertogradov, *arXiv preprint* [arXiv:2405.05370[gr-qc]].